Super-resolution Localization and Defocused Fluorescence Microscopy on Resonantly Coupled Single-Molecule, Single-Nanorod Hybrids

Liang Su,[†] Haifeng Yuan,*[,†] Gang Lu,[†] Susana Rocha,[†] Michel Orrit,[‡] Johan Hofkens,[†,§] and Hiroshi Uji-i*[,†,‖]

[†]Department of Chemistry, KU Leuven, Celestijnenlaan 200F, B-3001 Leuven, Belgium
[‡]LION, Huygens-Kamerlingh Onnes Laboratory, Leiden University, Niels Bohrweg 2, 2300RA Leiden, The Netherlands
[§]Nano-Science Center, University of Copenhagen, Universitetsparken 5, 2100 Copenhagen, Denmark
[‖]Research Institute for Electronic Science, Hokkaido University, N20W10, Kita-Ward, 001-0020 Sapporo, Japan

S *Supporting Information*

ABSTRACT: Optical antennas made of metallic nanostructures dramatically enhance single-molecule fluorescence to boost the detection sensitivity. Moreover, emission properties detected at the optical far field are dictated by the antenna. Here we study the emission from molecule–antenna hybrids by means of super-resolution localization and defocused imaging. Whereas gold nanorods make single-crystal violet molecules in the tip's vicinity visible in fluorescence, super-resolution localization on the enhanced molecular fluorescence reveals geometrical centers of the nanorod antenna instead. Furthermore, emission angular distributions of dyes linked to the nanorod surface resemble that of nanorods in defocused imaging. The experimental observations are consistent with numerical calculations using the finite-difference time-domain method.

KEYWORDS: *plasmon-enhanced fluorescence, gold nanorods, optical antennas, single molecules, super-resolution localization, defocused imaging*
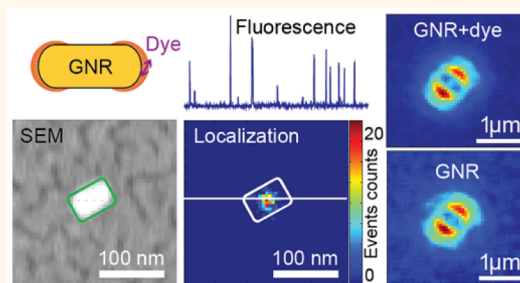
O ptical antennas, the counterparts of traditional radio and microwave antennas, are devices designed to efficiently convert freely propagating optical radiation into localized energy, and *vice versa.*[1,2] To operate at optical frequencies, optical antennas must possess characteristic dimensions on the same order as that of the light wavelength (hundreds of nanometers). Supporting localized surface plasmon metallic nanostructures made of gold or silver are excellent examples of optical antennas. On one hand, the highly concentrated electromagnetic fields generated in the antenna's near field can enhance excitation and facilitate photochemical reactions,[3] charge separation,[4] optical trapping,[5] catalysis,[6] and nonlinear optical phenomena.[7] Not only is the local light intensity increased dramatically compared to the incident light intensity, the local density of optical states (LDOS) around the antenna is altered, leading to altered radiative and nonradiative rates of emitters.[8,9] In this way, the emission properties, including intensity, quantum yield, and lifetime, can be modified.[9–11] On the other hand, radiation from emitters close to the antenna will be emitted to the far field *via* the antenna through efficient coupling. The antenna therefore dominates the emission of an efficiently coupled system. Hence, the emission properties in the far field, such as light directionality,[12] polarization, and spectra,[13,14] can be engineered using dedicated optical antennas. Many potential applications of optical antennas in photonics,[2,12,14,15] chemistry,[16–19] physics,[10,18,20–23] and biological science[24,25] have yet to be fully explored.

Although the fundamental concept of optical antennas is simple, experimental work, particularly with single molecules, is hindered by difficulties in manipulating and positioning individual molecules with respect to the antenna with molecular precision. Often relying on near-field manipulators,[8,15,18,26,27] statistics,[9,14,28] or chemical binding,[29–31] experimental observations on individual emitters interacting with optical antennas have yielded many essential insights. Attaching a spherical or
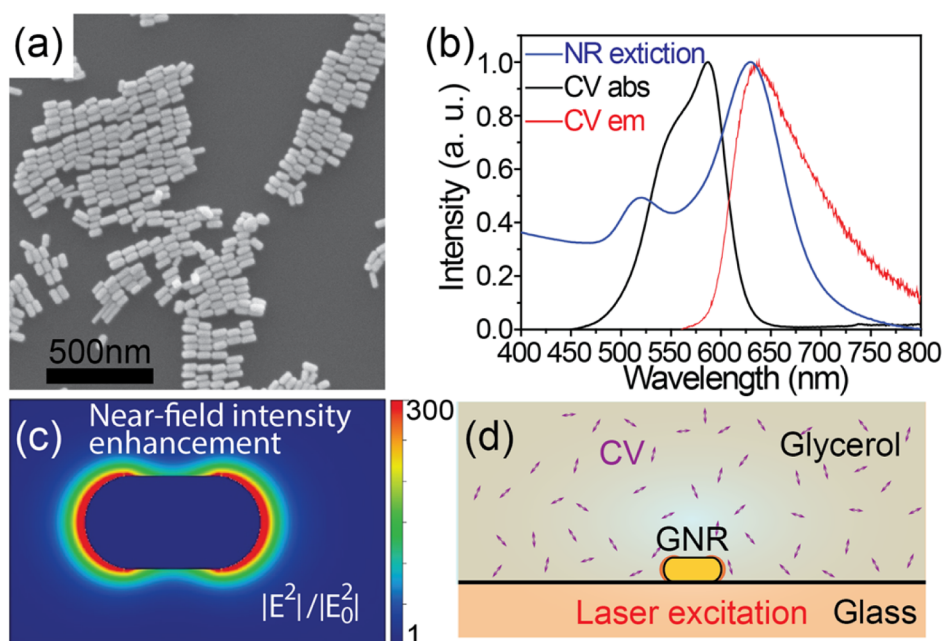
Figure 1. (a) SEM image of the synthesized gold nanorods. (b) Extinction spectrum (normalized) of a gold nanorod suspension in water (blue) and absorption (black) and emission (red) spectra of crystal violet in glycerol. (c) Calculated near-field optical intensity distribution around a single nanorod. The color bar represents the near-field intensity enhancement factors. (d) Schematic view of the experimental configuration. Double-ended arrows represent CV molecules in glycerol.

rod gold antenna onto a pointed probe, the groups of Novotny and Sandoghdar have revealed the strong spatial dependency of the interactions between single emitters and optical antennas.[8,18,27] Randomly doping dye molecules with a low fluorescence quantum yield in a thin polymer matrix around an array of gold bowtie antennas, Kinkhabwala *et al.* showed enormous fluorescence enhancements up to 1340-fold on single molecules and quantified changes over radiative and nonradiative rates of single emitters in the vicinity of gold bowtie antennas.[9] However, the above-mentioned methods can be applied only to immobile molecules. Employing specific molecular bindings to position single fluorophores at the tips of gold nanorods, Fu *et al.* demonstrated a strong enhancement of 40-fold on single-molecule fluorescence.[29] Nevertheless, DNA linkers placed between the fluorophores and antennas limit the accessible volume of the fluorophores. Recently, allowing dyes to diffuse in a viscous liquid medium, a 1000-fold enhancement was reported on single-molecule fluorescence using single-nanorod antennas.[10,16,32]

Because of its short range of some tens of nanometers, the interaction of an individual emitter with an optical antenna is difficult to characterize spatially using diffraction-limited far-field techniques. Super-resolution localization microscopy,[33] operating *via* the optical far field, however, can provide resolutions beyond the diffraction limit. It utilizes the stochastic nature of emissions from single quantum emitters to pinpoint individual emission events and thus to reconstruct structures[34,35] or interaction sites[36,37] with accuracies of tens of nanometers. Several super-resolution studies on molecule−metal−nanostructure hybrids[37−43] have revealed that the emission localization can be strongly influenced by interactions between molecules and the nanostructures. Weber *et al.* reported that super-resolution localization on molecule−nanostructure hybrids using surface-enhanced Raman spectroscopy (SERS) signals or fluorescence signals can result in noticeable differences in emission positions.[40] Recently, Su *et*

al. found that the metallic nanostructures with which the emitters are interacting can induce significant "distortions" of the point spread functions (PSFs), depending on nanostructure dimensions.[44] Blythe *et al.* demonstrated significant mismatches between nanorod dimensions revealed in super-resolution imaging and those revealed in AFM images of the same rods, regardless of the employed fitting models.[45] However, the understanding of the reported distortions and dimension mismatches remains elusive due to the lack of information about the antenna effect and the coupling between the emitter and the nanostructure, as indicated in a very recent report by Biteen's group.[46] Therefore, additional measures besides super-resolution localization have to be employed for a better understanding of the reported complex behavior of single emitters interacting with metallic nanostructures.

Relying on the anisotropic angular distribution of dipolar emission near the boundary of media with distinct refractive indices, defocused imaging allows one to visualize real-time changes in angular distributions of dipolar emission.[47−51] In a conventional imaging system, the dipole radiation pattern is projected into the detection plane and is focused to an Airy disk, which conceals the angular distribution of emission from an emitter. Deliberately introducing an aberration by slightly offsetting the dipole emitter away from the focal plane,[47,48] however, results in defocused patterns that reflect the emission angular distribution. Being sensitive to emission angular distributions, subtle changes in emission properties of molecule−antenna hybrids can be detected in a dynamic manner. Therefore, defocused imaging can potentially reveal how positions or orientations of individual molecular emitters influence the emission properties of the hybrid system *in situ*, where mobility of molecules is allowed. Resembling dipolar antennas, single-crystalline gold nanorods are simple and highly efficient optical antennas. The plasmon-related photoluminescence emission from nanorods,[52] particularly the emission that corresponds to the longitudinal plasmon resonance, resembles

dipolar emission.[53] Therefore, a nanorod's emission can be simulated and mapped using the dipolar model in defocused imaging.[48,54] Moreover, plasmonic and antenna properties of gold nanorods can be easily controlled by tuning their dimensions[10,55] *via* low-cost wet-chemical synthesis[56] or oxidative etching.[57]

Here, we apply super-resolution localization and defocused microscopy to investigate the coupling between single-molecule emitters and an individual gold nanorod optical antenna and to study the emission properties of the hybrid system in a dynamic fashion. Allowing weakly fluorescent molecules to diffuse in a viscous solvent, as reported in the literature,[10,16,32] we first apply super-resolution localization using conventional 2D Gaussian fitting on strongly coupled molecule–antenna hybrids. Moreover, we correlate the located emission events with the nanoantenna structure visualized in scanning electron microscopy (SEM). Combining with defocused imaging studies on fluorophores attached onto nanorods, we investigate the emission distribution dependence on molecule–antenna interactions. Furthermore, numerical calculations were carried out using the finite-difference time-domain (FDTD) method to understand the experimental findings.

RESULTS AND DISCUSSIONS

Super-resolution Localization Imaging on Gold Nanorod Antennas Surrounded with Crystal Violet (CV) in Glycerol. Gold nanorods synthesized using the seed-mediated method[58] show an average length of 69 ± 7 nm and an average diameter of 32 ± 5 nm in SEM micrographs (Figure 1a). Their extinction spectrum in aqueous solution shows two distinct peaks (Figure 1b, the blue curve). The peak around 520 nm corresponds to the transverse plasmon resonance. The other peak around 638 nm corresponds to the longitudinal plasmon resonance, which overlaps with the excitation laser wavelength (644 nm), the absorption (the black curve), and the emission spectra of CV (the red curve), as shown in Figure 1b. The overlapping spectra favor enhancement of the emission signal and ensure an efficient coupling of the emitter and the antenna.[10] Figure 1c shows the near-field optical intensity enhancement map around a gold nanorod.

CV was used here because of its low intrinsic fluorescence quantum yield and the large previously observed fluorescence enhancements of up to a thousand times.[32] Therefore, the fluorescence emission from molecules in the vicinity of nanorod tips can be easily distinguished from the constant background from unenhanced molecules in the focal volume and from nanorod photoluminescence. Moreover, the near-field volume, where the molecule's fluorescence is enhanced, is a few thousand times smaller than the focal volume, as shown in Figure 1c. Hence, the enhanced fluorescence emission from single molecules can be distinguished, even at high concentrations of nonenhanced molecules up to several micromolar.[16]

Here, we employed the same experimental configuration as reported in the literature,[10,32] as shown in Figure 1d. Gold nanorods were deposited on a glass cover slide and were then covered by a drop of 500 nM CV glycerol solution. A typical wide-field fluorescence image is shown in Figure 2a. Due to their constant photoluminescence, gold nanorods and fluorescent beads can be easily distinguished from the fluorescence background from CV molecules. Figure 2b shows a fluorescence time trace of a gold nanorod, a time trace of a fluorescent bead, and a time trace of the background. In contrast to constant fluorescence background from CV in
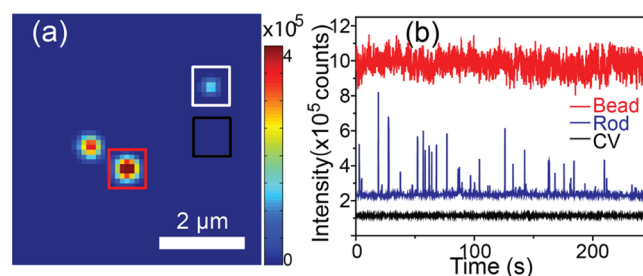

Figure 2. (a) Typical wide-field fluorescence image of a 5 μm × 5 μm area. The red square highlights a fluorescent bead. The white square highlights a gold nanorod. The black square highlights nonenhanced CV molecules in the background. The color bar represents the fluorescence intensity (counts per second). (b) Fluorescence time traces of the background (black), of the fluorescent bead (red), and of a gold nanorod (blue).

glycerol (in black color) and the almost constant bright fluorescence signal from the fluorescent bead (in red color), intense fluorescence bursts can be observed in the nanorod fluorescence time trace (in blue color). These fluorescence bursts are attributed to molecules whose emission is greatly enhanced in the vicinity of the single nanorod.[32] Serving as drift correction and correlation markers, fluorescent beads that show steady fluorescence can be easily distinguished from nanorods, which show intense fluorescence fluctuations in the presence of CV. Subtracting the constant background from nanorod photoluminescence and unenhanced CV molecules, the spatial photon distribution of each fluorescent burst was fitted using a 2D Gaussian function to locate the centroid of this emission.

After optical measurements, the sample was subjected to SEM measurements to correlate the fluorescence super-resolution images with their structures. The correlation was done using 100 nm fluorescent beads as alignment markers to project emission localizations on physical geometries of nanorods. Figure 3a shows a SEM image of a fluorescent bead, whose shape is outlined with a green circle. The corresponding localization image after drift correction is given in Figure 3b. The localization events over ten thousand frames showed a full-width at half-maximum (FWHM) of 13 nm, shown in Figure 3c. Figure 3d and g show SEM images on two closely positioned rods with different orientations. Their reconstructed localization images are given in Figure 3e and h, respectively. Both nanorods showed almost isotropic emission event distributions, but with different FWHMs of 13 and 27 nm. These values are comparable to the diameters of the nanorods and are smaller than the lengths of the rods. The different FWHMs are due to the different plasmon resonances of the nanorods, which lead to different enhanced burst intensities of CV molecules.[10] The localization precision of each localization event is determined by the fluorescence intensity of the burst event.[33] Therefore, bursts of lower fluorescence intensities have larger uncertainties of localization, thus showing broader distributions of localization events. The correlation between FWHMs of localization event distributions and the maximum enhanced fluorescence events on each nanorod is demonstrated in Figure S1.

To minimize the influence from distortions in the optical and SEM images, we overlaid localization images and SEM images only on an 8 μm × 8 μm area, in which at least two beads were present. We noticed that reconstructed centroids of the enhanced fluorescence from CV molecules were overlaid with
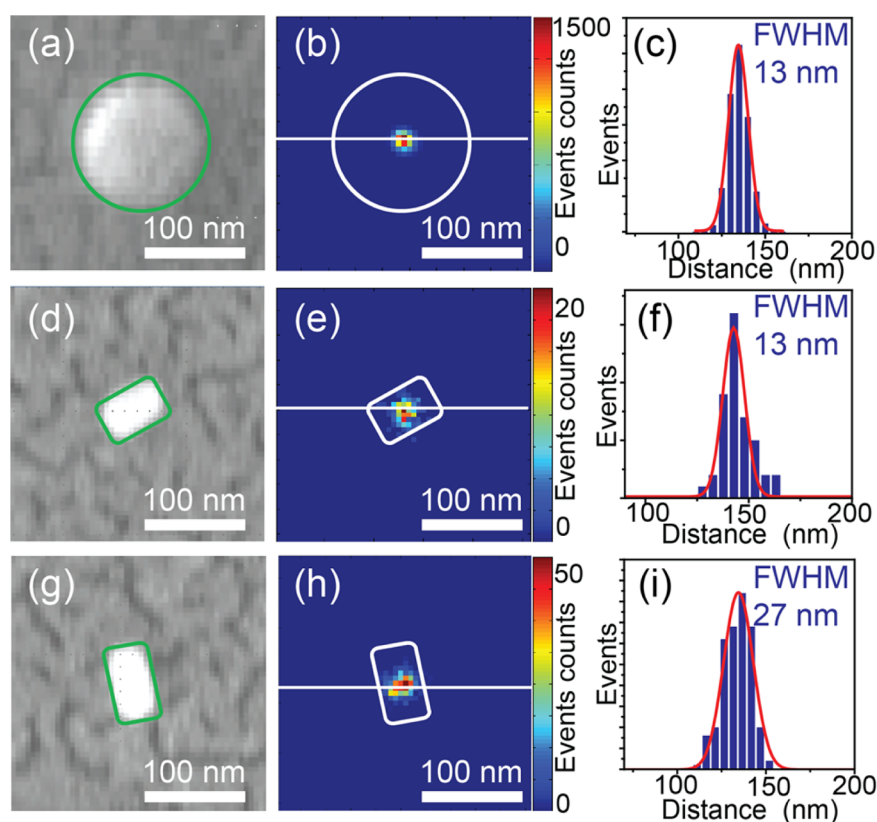
Figure 3. (a) SEM image of a fluorescent bead. The green circle highlights the outline of the bead. (b) Reconstructed super-resolution localization image of the same fluorescent bead. The white circle outlines the shape of the bead. The color bar represents the counts of events in each bin. (c) Profile of localization event distribution along the white solid line in (b). (d and g) SEM images of individual nanorods. (e and h) Localization images of the rods in (d) and (g), respectively. The color bars represent the counts of events in each bin. (f and i) Localization event distributions along the white solid lines in (e) and (h), respectively. The white and green blocks highlight the outline of the nanorods. The red solid lines are fitted Gaussian profiles.

the centers of gold nanorods, as shown in Figure 3e and h. The localization result is about 30 nm away from both tips of the nanorod, where the strong fluorescence enhancement occurs to result in discernible single-molecule fluorescence. Despite the crude estimation of the PSF we applied here, the observed far-field emission from centers of nanorods indicates that the emission from molecular emitters strongly couples into the antenna, while the fluorescence from emitters is largely enhanced.

FDTD on Super-resolution Localization of Enhanced CV Emission in the Vicinity of a Gold Nanorod. FDTD calculations were carried out on emission from molecule–antenna hybrids to understand the results in our experiments. The emission of the hybrid comes in two ways. On one hand, photoluminescence from a nanorod, a constant and reproducible background, can be easily eliminated by subtraction in each image frame. On the other hand, the molecular emission is altered by the nanorod antenna, which is the major contributing factor for the experimental observations in this work. In the following, we examine the influences of the nanorod antenna on the single-molecule emission by numerical calculations.

A dimensionless emissive dipole was used to model a dye molecule. The emitted light from the molecule was then monitored at an observation volume mimicking the detection configurations at the far field. To mimic the strong coupling, the dipole orientation was set to be parallel to the longitudinal axis of the nanorod. The distance between the dipole and the gold surface was chosen to be 5 nm in order to simulate the

circumstances of strong fluorescence enhancements.[8,10] Three position configurations, shown in Figure 4, were examined, respectively, a dipole at the tip (position 1), at the corner (position 2), and at the side (position 3) of a nanorod. The calculated PSFs of single molecules under the three circumstances show little differences that can hardly be noticed in Figure 4a–c. The interaction of the molecule's emission with the nanorod is better visualized in the optical near field. Figure 4d–f illustrate the near field around the molecule–nanorod hybrids of the three configurations, showing the disturbed molecular emission near-field distribution by the nanorod.

Localization inaccuracies inherent to conventional 2D Gaussian fitting were then evaluated by applying 2D Gaussian fitting on the calculated PSFs. The localization results are compared with the actual positions of emitters in Figure 4g–i, where red diamonds represent the actual positions of emitters, black crosses represent the localization events based on 2D Gaussian approximation, and blue dots pinpoint the centers of nanorods. At position 1, the localization position on the molecular fluorescence shows an approximately 8 nm offset from the center of the nanorod along the longitudinal direction, as illustrated in Figure 4g. The molecular emission at position 2 was localized at a position 5 nm from the nanorod center along the transverse direction. For the molecule at position 3, the localization was within 3 nm from the center of the nanorod. Deviations on the localization positions from the center position of the nanorod are less than 10 nm for other circumstances with different in-plane dipole orientations.
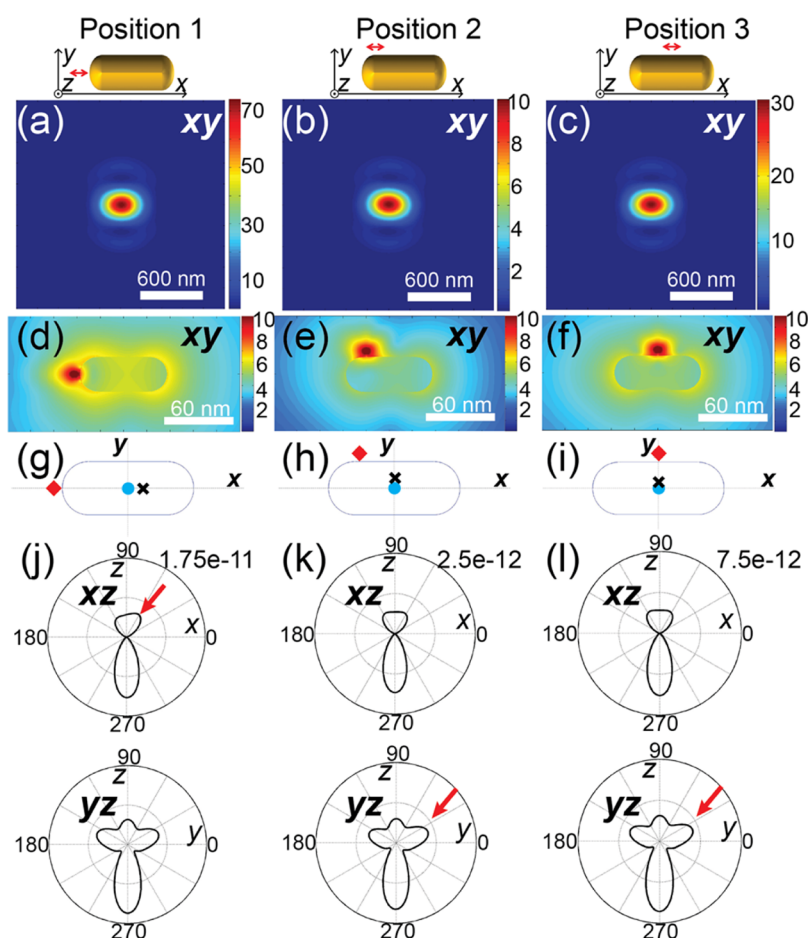
Figure 4. (a−c) Calculated PSFs for different dye positions in regard to the nanorod, illustrated in the drawings on top of each plot. (d−f) Near-field distributions of molecular emission around the nanorod at three different dye positions. (g−i) Localization results using a 2D Gaussian PSF approximation on the three circumstances shown in (a), (b), and (c), respectively. Red diamonds, black crosses, and cyan dots are used to represent the actual position of the fluorophore, the localized events using 2D Gaussian, and the center position of the nanorod, respectively. (j−l) Emission angular distributions in the xz and yz plane from the molecule−antenna hybrids with different configurations in (a)−(c), respectively. The red arrows highlight the asymmetric distribution that leads to the off-center localization.

Moreover, the localization results show different offset directions from centers of nanorods. Figure 4g shows an offset opposite the side where the emitter locates, whereas the localization positions in Figure 4h and i show offsets toward the emitters.

The localization errors revealed in the above are consequences of the asymmetric emission angular distributions toward the far field from the hybrids. The angular distribution of emitted light eventually determines the pixelated intensity profile imaged at the fixed detection plane and thus strongly influences the localization result.[59] Figure 4j−l illustrate the emission angular distributions that correspond to the three position configurations. The emitter at position 1 shows an emission angular distribution that is asymmetric in the xz plane but symmetric in the yz plane, as shown in Figure 4j. The lopsided emission along the longitudinal axis of the nanorod results in the localization offset from the nanorod center toward the direction opposite the emitter side. The emitters at position 2 and position 3, however, show significant asymmetry in the yz plane but little asymmetry in the xz plane, as demonstrated in Figure 4k and l, respectively. As a result, the localization positions on emitters at position 2 and position 3 shift correspondingly along the transverse direction toward the side where the emitters locate.

Therefore, we summarize the above FDTD results in two ways. (i) The emission collected at the far field reflects the position of the antenna instead of position of the emitter, demonstrating antenna coupling. (ii) 2D Gaussian approximation on the PSF results in localization errors up to 10 nm. Thus, the localization events will span over an area within 20 nm. The estimated localization inaccuracy, which agrees with the localization event distributions (FWHMs ranging from 13 to 30 nm) revealed in our experiment, is comparable to the nanorod diameter but is less than the nanorod length.

Defocused Imaging of Gold Nanorod Antennas Labeled with Alexa647 in Aqueous Buffer Solution. We further verified the role of antenna coupling in emission to the far field by defocused fluorescence imaging. Although CV molecules in glycerol can yield largely enhanced fluorescence signals, the total number of photons in each fluorescence burst is not sufficient to produce clear defocused patterns as the emitted photons are divided onto many pixels in defocused imaging. Moreover, the dwell time of a CV molecule in the near-field volume is short.[16] Furthermore, photobleaching of CV molecules takes place in several hundred milliseconds,[16] contributing to a limited number of photons in each burst. In order to overcome the aforementioned experimental limitations for defocused imaging, Alexa647 molecules were tethered onto
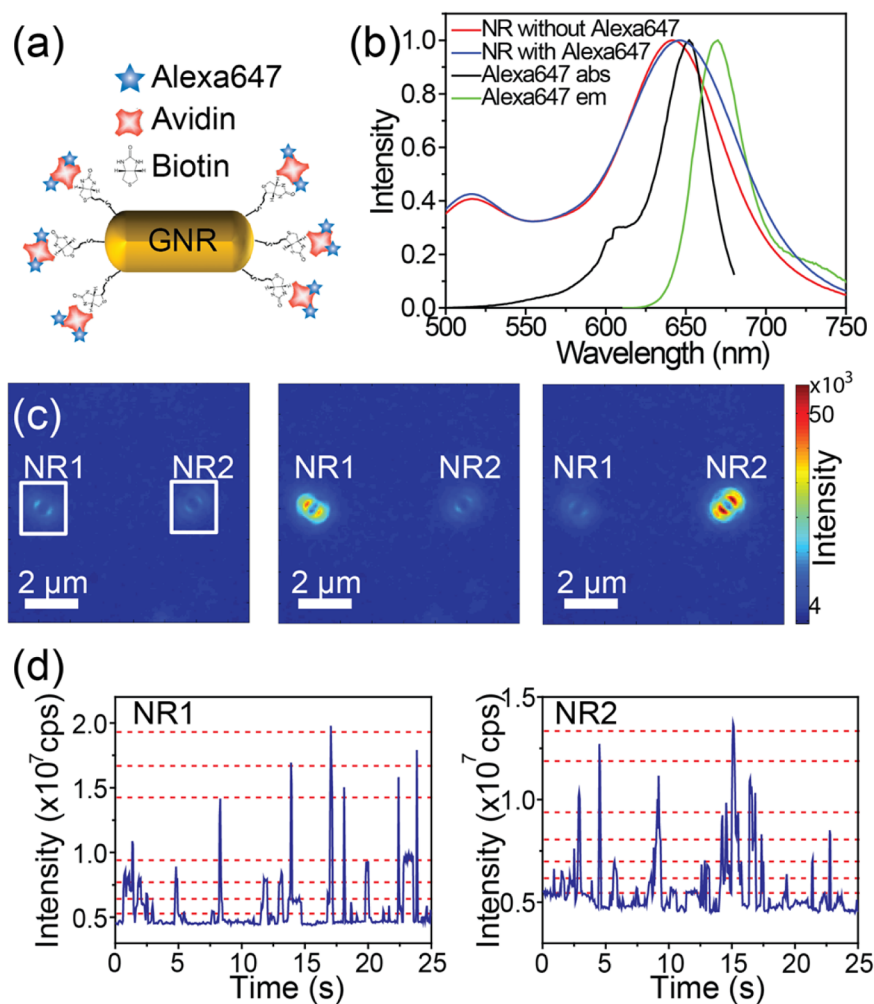
Figure 5. (a) Schematic view of a gold nanorod labeled with Alexa647. (b) Extinction spectra of gold nanorods before and after label attachment (red and blue, respectively) and the absorption spectrum (black) and the emission spectrum (green) of Alexa647. (c) Snapshots of two defocused patterns at different times. The two nanorods show random blinking events. (d) Fluorescence intensity time traces of the nanorods highlighted with white squares in (c). The stochastic blinking of each fluorophore on the nanorods leads to discrete intensity levels in the fluorescence time trajectories, from which we can estimate the number of fluorophores on each nanorod. The red dashed lines are a guide to the eye to indicate the aforementioned intensity levels.

the surfaces of gold nanorods using thiolated biotine and dye–avidine conjugates as illustrated in Figure 5a. Low concentrations of chemicals and rods were employed to avoid rod–rod linkage due to the multiple binding pockets of avidin. The distance between fluorophore and the gold surface is estimated to be 5–7 nm. Alexa647 was employed for the following reasons: (i) Its emission spectrum overlaps with the longitudinal plasmon resonances of gold nanorods (Figure 6b); (ii) Alexa647 is known to blink under certain buffer conditions, resulting in its wide application in single-molecule super-resolution microscopy;[44,60] (iii) Alexa647 has a higher fluorescence quantum yield (0.33) and is more photostable than CV. Upon labeling, the extinction spectrum of labeled nanorods showed a 5 nm red-shift in the longitudinal peak (Figure 5b), indicating an increased local refractive index around the nanorods.[61]

The labeling yield and the labeling density were low, which is evident from the fact that many nanorods showed steady photoluminescence intensity without fluorescence blinking. In addition, the blinking nanorods showed limited numbers of blinking events before bleaching of Alexa647. Moreover, the surfactant's low binding affinity at nanorod tips due to gold

surface atomic alignments and surface curvatures makes the nanorod tips more likely to be exposed for binding of thiolated biotin molecules at low cetyltrimethylammonium bromide (CTAB) concentrations.[57,61] Therefore, we can safely assume that the majority of fluorophores are attached close to the tips of nanorods in our experiment.

On moving the focal plane ~1 μm away from the sample, defocused fluorescence imaging video streams were recorded over laser-illuminated sample areas. Figure 5c shows three sequential frames on the same sample area, in which two defocused patterns can be clearly identified. Their different relative intensities in these frames indicate that the fluorophores on each nanorod were blinking stochastically. Each bright pattern in Figure 5c represents a nanorod. The defocused patterns orient along different directions, indicating the orientations of the nanorods.[54] We found that approximately 70% of the nanorods showed fluorescence blinking within our measurement time, indicating the presence of Alexa647 dyes in their vicinity. Figure 5d shows fluorescence intensity time traces of two Alexa647–nanorod hybrids highlighted with squares in Figure 5c. After several digital blinking events, the fluorescence signals from Alexa647 vanished without recovery, leaving a
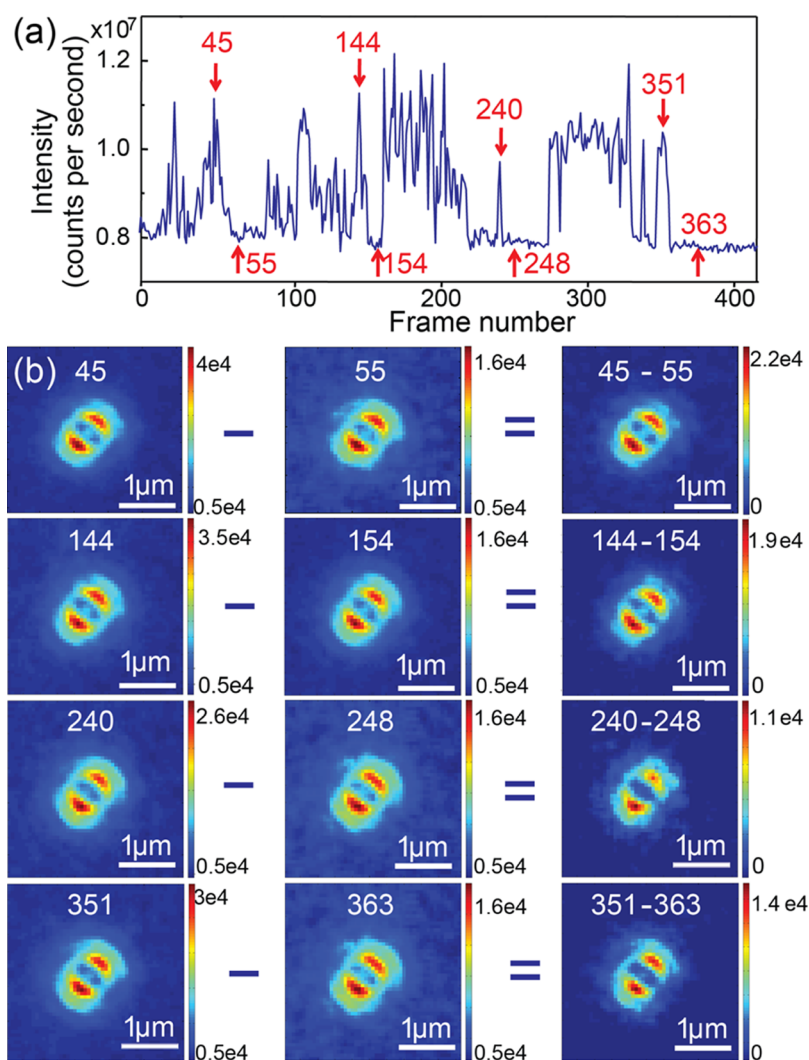
Figure 6. (a) Fluorescence intensity time trace of a single nanorod labeled with Alexa647 in the switching buffer. The red arrows and the associated numbers indicate the frame numbers of selected images. (b) Set of defocused patterns obtained from fluorescence bursts and from background in the frames highlighted in (a). Patterns in the right column are obtained by subtracting the patterns in the middle column (nanorod photoluminescence patterns) from the patterns in the left column (patterns of total intensities). The corresponding frame numbers are given on top of each defocused pattern. The color bars represent fluorescence intensities.

strong and steady background of nanorod photoluminescence. These digital and stochastic blinking events of Alexa647 in the switching buffer indicated that at most one fluorophore emitted most of the time. Moreover, the same Alexa647−nanorod hybrid showed large variations in blinking intensities. This is most likely due to different labeling positions of Alexa647 with respect to the nanorod. Fluorophores at different positions experienced different excitation and emission environments, which led to their different emission intensities. We estimated the number of fluorophores on the labeled nanorods to be less than 8 from the discrete intensity levels observed in the fluorescence time traces. The discrete intensity levels are marked with red dashed lines (guide to eye) in Figure 5d.

We now compare the defocused pattern due to molecular emission and that of nanorod photoluminescence. Thanks to the fluorescence blinking of Alexa647, photoluminescence and molecular fluorescence can be distinguished in defocused imaging time sequences. A typical fluorescence intensity time trace of an Alexa647−nanorod hybrid is given in Figure 6a. The time trace showed active blinking of signal intensities between 8 × 10^6 and 10^7 counts per second. The blinking amplitude,

about 2×10^6 counts per second, is attributed to Alexa647 molecules on the nanorod. The steady background of about 8×10^6 counts per second originates from nanorod photoluminescence. Figure 6b shows the defocused patterns at different time points highlighted with arrows in Figure 6a. The frame numbers of each snapshot were denoted next to the red arrows in Figure 6a. Defocused patterns while the molecular emission was on (frames 45, 144, 240, and 351) are given in the left column of Figure 6b. The middle column shows defocused patterns of the nanorod photoluminescence (frames 55, 154, 248, and 363). Subtracting nanorod photoluminescence from the total signal, the right column in Figure 6b shows the defocused patterns corresponding to fluorescence emission from Alexa647. We point out that defocused patterns of molecular emission closely resemble that of nanorod photoluminescence.

Next, we discuss possible reasons that the sequenced images show almost identical emission patterns in our defocused measurements. First of all, we exclude the case in which the fluorophores' transition dipole moments were aligned parallel with the longitudinal axis of the nanorod. Although tethered
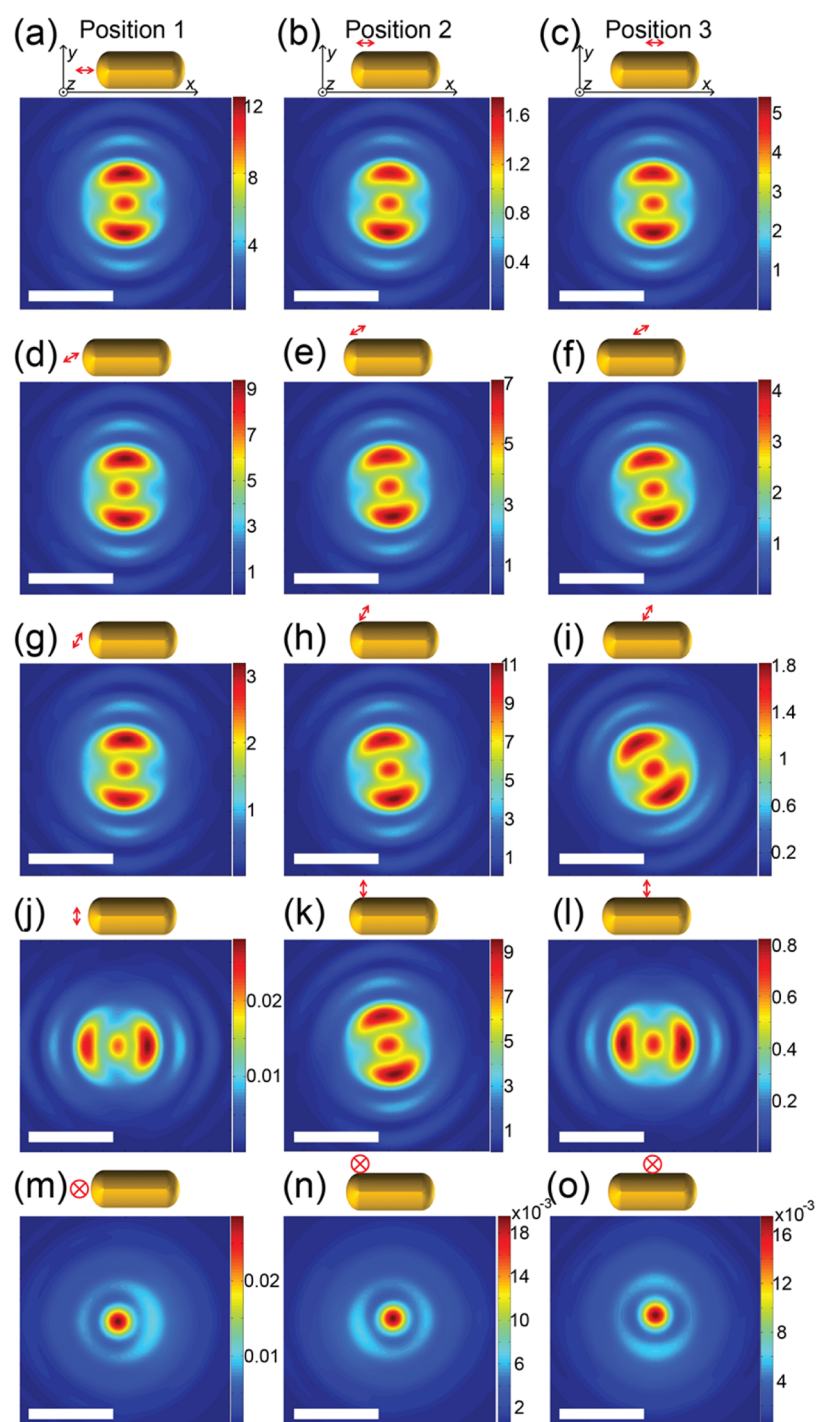
Figure 7. (a−l) Simulated far-field defocused patterns of the single nanorod antenna systems with emissive dipoles with different in-plane orientations with respect to the nanorod. The color scales are normalized to the maximum intensities in each plot. (m−o) Simulated far-field defocused patterns of the single-nanorod antenna system with emissive dipoles oriented perpendicular to the sample plane at various positions. The color scales are normalized to the maximum intensities in each plot. The arrow represents the location and orientation of the emitter. The yellow rounded shape indicates the gold nanorod.

onto nanorods, the fluorophores are able to orientate because of the flexible nature of the conjugations used as linkers. Therefore, orientations of fluorophores on nanorods are most likely random instead of being fixed to align with the nanorods. Second, a few fluorophores are attached onto each nanorod at different positions, as indicated by blinking events of multiple intensity levels in Figure 5d and e. As a result, defocused pattern sequences collect contributions from fluorophores at different positions. Although the enhanced fluorescence intensities are strongly biased by the molecule's relative orientation and position with respect to the nanorod, all defocused patterns showed negligible changes along with fluctuations of fluorescence intensities, indicating that emission patterns observed at far field were insensitive to the positions and orientations of the emissive fluorophore. Hence, the identical emission patterns of molecular fluorescence and

nanorods' photoluminescence observed in our experiment are most likely due to the antenna coupling of the molecule's emission with the nanorod antenna. By efficient and resonant coupling, the optical antenna dictates the emission patterns from molecular emitters in its close vicinity.

FDTD on Defocused Patterns of Dye-Labeled Gold Nanorods. We then apply FDTD numerical calculations on far-field defocused patterns of the coupled molecule−antenna hybrid to reveal how the molecule's relative positions and orientations influence the observed defocused patterns. We calculated the defocused patterns from molecule−antenna hybrids under realistic conditions in our experiment. We simulated a few representative relative positions and orientations of the molecule−antenna hybrid system as illustrated in Figure 7. A point-like electric dipole, represented using a double-ended arrow in Figure 7, was used to simulate an emissive molecule. The directions of the arrow represent the dipole orientation. The electric dipole was placed 5 nm away from the surface of a gold nanorod at three different locations, the center of the tip region (position 1), the side of the tip region (position 2), and the middle of the nanorod's cylindrical wall (position 3). At each dipole location, five dipole orientations were examined, $0°$, $30°$, $60°$, and $90°$ in-plane and $90°$ out-of-plane with respect to the nanorod. The numerical calculation results are given right beneath each schematic view of the configurations in Figure 7. It is worth noting that different color scales are applied in each plot to enhance the visualization of the defocused patterns. When the molecular dipole is at the center of the tip and is parallel to the nanorod, the gap of the defocused fluorescence pattern is aligned along the nanorod's longitudinal axis, which resembles the defocused pattern of the nanorod photoluminescence. However, when changing the orientation of the molecular dipole, the fluorescence emission pattern alters and the fluorescence intensity decreases. We notice that the defocused fluorescence pattern is the most sensitive to the dipole orientation when the molecule is positioned along the axis close to the tip (position 1 in Figure 7). As shown in the left column of Figure 7a, a $0°$ to $90°$ in-plane reorientation can lead to a $90°$ rotation of the defocused pattern and to an intensity decrease by a factor of more than 600. When the molecule is positioned sideways close to the nanorod tip (position 2 in Figure 7), a $0°$ to $90°$ in-plane reorientation rotates the defocused pattern by $20°$ and shows about a 10-fold difference in intensities. In another circumstance where the molecule is positioned close to the middle of the cylindrical wall of a nanorod (position 3 in Figure 7), a $0°$ to $90°$ in-plane reorientation results in a $90°$ difference in the defocused pattern, but the intensity is reduced by a factor of 50. It is also worth noting that when the dipole is $90°$ out-of-plane with respect to the rod, the defocused patterns possess no feature of the rod, indicating little coupling of the emitter to the antenna. These simulation results confirm that defocused patterns strongly depend on emitters' positions and orientations related to the nanorod antenna. Moreover, the sensitivity of defocused patterns on the emitter's orientation differs at different locations. When the emitter is located at the center of a nanorod's tip, the defocused pattern is most sensitive on the emitter's different orientations.

Besides the numerical simulations of the emission process, it is necessary to take the excitation process into account. This is because the excitation intensities experienced by molecules in the vicinity of a nanorod strongly depend on their positions

relative to the nanorod. At the plasmon resonance, a nanorod can create several hundred times intensity enhancement at the tips along the longitudinal direction. Therefore, a molecule at the tip region with an orientation parallel to the nanorod's longitudinal direction can experience up to 100 times stronger excitation compared to molecules located at the middle of the cylindrical wall.

The defocused patterns depend on the molecule's position and orientation in two distinct ways. The first one is through the emission process, where the antenna coupling strongly depends on the relative positions and orientations of the molecule and the nanorod. The second one is through the excitation process, which involves the near-field intensity distributions. In particular, the strongest coupling configuration, in which a molecule is positioned on the axis and close to the tip of a nanorod, also gives rise to the strongest excitation intensity. As a result, such a strongly coupled system produces the strongest fluorescence signal in defocused imaging, which is several orders of magnitude stronger than that from other positions and orientations. In addition, the strong photo-luminescence background in our experiment was almost as strong as fluorescence from the probe molecule. Therefore, defocused patterns from cases other than the strongly coupled one are difficult to distinguish even with efficient emitting fluorophores. Hence, the observed fluorescence is mostly from the emitter that couples to the nanorod antenna efficiently, which gives a radiation pattern dominated by the antenna.

CONCLUSIONS

In this work, we demonstrated a novel approach, combining super-resolution localization, correlative SEM, and defocused imaging, to study molecule−antenna hybrids at the single-molecule, single-antenna level. Allowing weakly fluorescent dye molecules to freely diffuse in a viscous medium, sufficient statistics can be built up to determine the image centroids of in-plane-aligned molecular−antenna hybrids with a 30 nm resolution using a 2D-Gaussian-approximated PSF. Correlating super-resolution localization events and SEM micrographs, we found the individual isotropic centroids located at the geometrical centers of individual nanorods, while the dyes are supposed to be excited in the vicinity of the nanorod tips. Moreover, defocused microscopy on chemically labeled molecule−antenna hybrids unraveled the dominating role of the nanorod antenna in the coupled molecular emission to the optical far field. Such observations emphasize the nanorod's dual roles to enhance fluorescence signals and to dominate the fluorescence emission at the far field *via* efficient coupling. Our results emphasize the role of plasmonic nanostructures as optical antennas in the plasmon-enhanced microscopy on a resonantly coupled optical system. The antenna effects have to be considered in optical and spectroscopic studies of interactions between molecules and metallic nanostructures, particularly in super-resolution studies.

MATERIALS AND METHODS

Gold Nanorod Synthesis. All chemicals were purchased from Sigma-Aldrich and were used as received. The synthesis was carried out in Milli-Q water. Seeds: 6.4 mg of sodium borohydride ($NaBH_4$) was dissolved in 10 mL of ice-cold water right before use. A 25 μL amount of 100 mM $HAuCl_4$ was added into 10 mL of 0.1 M CTAB solution. While vigorously stirring the mixture, we injected 0.6 mL of ice-cold $NaBH_4$ solution, while the color of the mixture changed from golden to brownish-yellow. After vigorous stirring for 60 s, the solution

was left at room temperature for 2 h. The nanoparticles of this solution were later used as seeds to initiate the growth process.

Growth. A 25 μL amount of 100 mM HAuCl$_4$ was mixed with 5 mL of 0.1 M CTAB solution. After addition of various amounts of 20 mM AgNO$_3$, 27.5 μL of 100 mM ascorbic acid was added to the growth solution, leading to a color change from golden yellow to colorless. The final step was to add various amount of the seed solution into the growth solution. Leaving the solution at 28 °C, the color of these solutions gradually changed within 60 min.

Sample Preparation for Super-resolution Localization Microscopy. A 50 μL gold nanorod suspension in 100 μM CTAB was spin-coated on a glass coverslide and washed three times to remove the CTAB. A 30 min UV/ozone treatment followed to further remove the residues. After the sample was mounted onto the microscope, the nanorods were immersed into a 500 nM crystal violet solution in glycerol.

Labeling Nanorods with Alexa647. The gold nanorods were centrifuged and redispersed in a Milli-Q water solution of biotin-terminated poly(ethylene glycol) (2.5 mM, Nanoscience Instruments). During this process, the CTAB concentration was kept around 200 μL to prevent aggregation of gold nanorods. After shaking overnight, Alexa647-conjugated streptavidin (Life Technologies) was added. The mixture was then kept for at least 2 h. Afterward, the excess fluorophore in solution was removed by centrifugation at 4000 rpm.

Sample Preparation for Defocused Imaging on Alexa647-Labeled Nanorods. The solution was then spin-cast onto a coverslip. After that, the sample was kept in a sealed chamber filled with switching buffer, phosphate-buffered saline (pH 7.4), containing oxygen scavenger (0.5 mg/mL glucose oxidase (Sigma-Aldrich), 40 mg/mL catalase (Roche Applied Science), 10% w/v glucose) and 50 mM 2-mercaptoethylamine.

Single-Molecule Fluorescence Microscopy. Wide-field fluorescence microscopy was carried out on an inverted optical microscope (Ti-U, Nikon) equipped with a 100× oil immersion objective (NA = 1.49, CFI Plan, Nikon) and a cooled electron multiplying charge-coupled device (EM-CCD) camera (ImagEM, Hamamatsu). Collimated 644 nm circularly polarized light from a solid-state laser (Cobolt) was focused at the back focal plane of the objective as the excitation source. Emission was collected with the same objective and imaged with the EM-CCD camera after passing through a dichroic mirror (z633rdc, Chroma) and a long-pass filter (HQ655LP, Chroma). The image was further magnified 2.5 times with a camera lens before the EM-CCD camera, resulting in a maximum field of view of 32.8 μm × 32.8 μm (64 nm × 64 nm per pixel). The acquisition time was 50 ms.

Data Analysis. Super-resolution localization was done with a homemade Matlab code. Sample drifts were corrected using the positions of fluorescent beads in each image frame. For drift correction of the setup, fluorescent beads that emit constantly in all frames are used. Because of their strong emission, their positions can be determined with high accuracy. Applying 2D Gaussian fitting fluorescence signals, the coordinates of the beads were traced as a function of time. These trajectories reflect mechanical drifts of the sample during data acquisition. The sample drift in each frame can thus be deduced from the mean trajectory of beads, and in this way the coordinates of fluorescence burst events in each frame can be corrected. The coordinates after drift corrections were used to reconstruct the single-molecule super-resolution images. To achieve an accurate drift correction, the density of fluorescent beads was controlled to guarantee there are at least several beads in an area of 10 × 10 μm^2.

SEM. The sample was coated with a thin gold film using a JEOL auto fine film coater prior to SEM measurements. SEM micrographs were recorded using a FEI FEG-250 scanning electron microscope.

FDTD Calculation. The finite-difference time-domain method was used to numerically calculate the angular distribution of the far-field scattering of molecular fluorescence in the vicinity of the gold nanorods (Lumerical Solution Inc., Vancouver, Canada). The tabled values of Johnson and Christy were used for the dielectric function of gold.[62] The rod was placed on a dielectric slab with a refractive index

of 1.5 (simulating a glass coverslip). The surroundings were set to a refractive index of 1.33 to simulate the buffer or a refractive index of 1.47 to simulate glycerol. A single fluorescence molecule was modeled as an oscillating electric dipole at 5 nm away from the nanorod surface. To mimic the image acquisition, a monitor volume was set at the high refractive index side. The monitor volume was chosen to fully cover the region from which our objective (NA = 1.49) collects light. In this way, the Poynting vector (the energy flow) calculated at this monitor volume simulates the experimentally acquired image. The point spread function was calculated by conducting a Fourier transform of the Poynting vector collected on the monitor volume.

ASSOCIATED CONTENT

Ⓢ Supporting Information

The Supporting Information is available free of charge on the ACS Publications website at DOI: 10.1021/acsnano.5b07294.

> Correlation between the FWHMs of localization events' distribution measured on each nanorod and their maximum fluorescence burst intensities (PDF)

AUTHOR INFORMATION

Corresponding Authors
*E-mail: haifeng.yuan@chem.kuleuven.be.
*E-mail: hiroshi.ujii@es.hokudai.ac.jp.

Notes
The authors declare no competing financial interest.

REFERENCES

(1) Bharadwaj, P.; Deutsch, B.; Novotny, L. Optical Antennas. *Adv. Opt. Photonics* 2009, *1*, 438−483.

(2) Novotny, L.; van Hulst, N. Antennas for Light. *Nat. Photonics* 2011, *5*, 83−90.

(3) Zhou, X.; Deeb, C.; Kostcheev, S.; Wiederrecht, G. P.; Adam, P. M.; Beal, J.; Plain, J.; Gosztola, D. J.; Grand, J.; Felidj, N.; Wang, H.; Vial, A.; Bachelott, R. Selective Functionalization of the Nanogap of a Plasmonic Dimer. *ACS Photonics* 2015, *2*, 121−129.

(4) Tian, Y.; Tatsuma, T. Mechanisms and Applications of Plasmon-Induced Charge Separation at TiO$_2$ Films Loaded with Gold Nanoparticles. *J. Am. Chem. Soc.* 2005, *127*, 7632−7637.

(5) Juan, M. L.; Righini, M.; Quidant, R. Plasmon Nano-Optical Tweezers. *Nat. Photonics* 2011, *5*, 349−356.

(6) Zhong, Y.; Ueno, K.; Mori, Y.; Shi, X.; Oshikiri, T.; Murakoshi, K.; Inoue, H.; Misawa, H. Plasmon-Assisted Water Splitting Using Two Sides of the Same SrTiO3 Single-Crystal Substrate: Conversion of Visible Light to Chemical Energy. *Angew. Chem., Int. Ed.* 2014, *53*, 10350−10354.

(7) Kauranen, M.; Zayats, A. V. Nonlinear Plasmonics. *Nat. Photonics* 2012, *6*, 737−748.

(8) Anger, P.; Bharadwaj, P.; Novotny, L. Enhancement and Quenching of Single-Molecule Fluorescence. *Phys. Rev. Lett.* **2006**, *96*, 113002.

(9) Kinkhabwala, A.; Yu, Z. F.; Fan, S. H.; Avlasevich, Y.; Mullen, K.; Moerner, W. E. Large Single-Molecule Fluorescence Enhancements Produced by a Bowtie Nanoantenna. *Nat. Photonics* **2009**, *3*, 654−657.

(10) Khatua, S.; Paulo, P. M. R.; Yuan, H. F.; Gupta, A.; Zijlstra, P.; Orrit, M. Resonant Plasmonic Enhancement of Single-Molecule Fluorescence by Individual Gold Nanorods. *ACS Nano* **2014**, *8*, 4440−4449.

(11) Puchkova, A.; Vietz, C.; Pibiri, E.; Wuensch, B.; Sanz Paz, M.; Acuna, G. P.; Tinnefeld, P. DNA Origami Nanoantennas with over 5000fold Fluorescence Enhancement and Single-Molecule Detection at 25 μM. *Nano Lett.* **2015**, *15*, 8354.

(12) Curto, A. G.; Volpe, G.; Taminiau, T. H.; Kreuzer, M. P.; Quidant, R.; van Hulst, N. F. Unidirectional Emission of a Quantum Dot Coupled to a Nanoantenna. *Science* **2010**, *329*, 930−933.

(13) Kuehn, S.; Mori, G.; Agio, M.; Sandoghdar, V. Modification of Single Molecule Fluorescence Close to a Nanostructure: Radiation Pattern, Spontaneous Emission and Quenching. *Mol. Phys.* **2008**, *106*, 893−908.

(14) Ren, M.; Chen, M.; Wu, W.; Zhang, L.; Liu, J.; Pi, B.; Zhang, X.; Li, Q.; Fan, S.; Xu, J. Linearly Polarized Light Emission from Quantum Dots with Plasmonic Nanoantenna Arrays. *Nano Lett.* **2015**, *15*, 2951−2957.

(15) Taminiau, T. H.; Stefani, F. D.; Segerink, F. B.; Van Hulst, N. F. Optical Antennas Direct Single-Molecule Emission. *Nat. Photonics* **2008**, *2*, 234−237.

(16) Khatua, S.; Yuan, H.; Orrit, M. Enhanced-Fluorescence Correlation Spectroscopy at Micro-Molar Dye Concentration around a Single Gold Nanorod. *Phys. Chem. Chem. Phys.* **2015**, *17*, 21127−21132.

(17) Wientjes, E.; Renger, J.; Curto, A. G.; Cogdell, R.; van Hulst, N. F. Strong Antenna-Enhanced Fluorescence of a Single Light-Harvesting Complex Shows Photon Antibunching. *Nat. Commun.* **2014**, *5*, 4236.

(18) Bharadwaj, P.; Beams, R.; Novotny, L. Nanoscale Spectroscopy with Optical Antennas. *Chem. Sci.* **2011**, *2*, 136−140.

(19) Punj, D.; Regmi, R.; Devilez, A.; Plauchu, R.; Moparthi, S. B.; Stout, B.; Bonod, N.; Rigneault, H.; Wenger, J. Self-Assembled Nanoparticle Dimer Antennas for Plasmonic-Enhanced Single-Molecule Fluorescence Detection at Micromolar Concentrations. *ACS Photonics* **2015**, *2*, 1099−1107.

(20) Lu, G. W.; Liu, J.; Zhang, T. Y.; Li, W. Q.; Hou, L.; Luo, C. X.; Lei, F.; Manfait, M.; Gong, Q. H. Plasmonic Near-Field in the Vicinity of a Single Gold Nanoparticle Investigated with Fluorescence Correlation Spectroscopy. *Nanoscale* **2012**, *4*, 3359−3364.

(21) Muskens, O. L.; Giannini, V.; Sanchez-Gil, J. A.; Rivas, J. G. Strong Enhancement of the Radiative Decay Rate of Emitters by Single Plasmonic Nanoantennas. *Nano Lett.* **2007**, *7*, 2871−2875.

(22) Farahani, J. N.; Pohl, D. W.; Eisler, H. J.; Hecht, B. Single Quantum Dot Coupled to a Scanning Optical Antenna: a Tunable Superemitter. *Phys. Rev. Lett.* **2005**, *95*, 017402.

(23) Neumann, L.; van 't Oever, J.; van Hulst, N. F. A Resonant Scanning Dipole-Antenna Probe for Enhanced Nanoscale Imaging. *Nano Lett.* **2013**, *13*, 5070−5074.

(24) Lu, G.; De Keersmaecker, H.; Su, L.; Kenens, B.; Rocha, S.; Fron, E.; Chen, C.; Van Dorpe, P.; Mizuno, H.; Hofkens, J.; Hutchison, J. A.; Uji-i, H. Live-Cell SERS Endoscopy Using Plasmonic Nanowire Waveguides. *Adv. Mater.* **2014**, *26*, 5124−5128.

(25) Adato, R.; Yanik, A. A.; Amsden, J. J.; Kaplan, D. L.; Omenetto, F. G.; Hong, M. K.; Erramilli, S.; Altug, H. Ultra-sensitive Vibrational Spectroscopy of Protein Monolayers with Plasmonic Nanoantenna Arrays. *Proc. Natl. Acad. Sci. U. S. A.* **2009**, *106*, 19227−19232.

(26) Novotny, L.; Stranick, S. J. Near-Field Optical Microscopy and Spectroscopy with Pointed Probes. *Annu. Rev. Phys. Chem.* **2006**, *57*, 303−331.

(27) Kuehn, S.; Hakanson, U.; Rogobete, L.; Sandoghdar, V. Enhancement of Single-Molecule Fluorescence Using a Gold Nanoparticle as an Optical Nanoantenna. *Phys. Rev. Lett.* **2006**, *97*, 017402.

(28) Munechika, K.; Chen, Y.; Tillack, A. F.; Kulkarni, A. P.; Plante, I. J. L.; Munro, A. M.; Ginger, D. S. Spectral Control of Plasmonic Emission Enhancement from Quantum Dots near Single Silver Nanoprisms. *Nano Lett.* **2010**, *10*, 2598−2603.

(29) Fu, Y.; Zhang, J.; Lakowicz, J. R. Plasmon-Enhanced Fluorescence from Single Fluorophores End-Linked to Gold Nanorods. *J. Am. Chem. Soc.* **2010**, *132*, 5540−5541.

(30) Zhang, T.; Gao, N.; Li, S.; Lang, M. J.; Xu, Q.-H. Single-Particle Spectroscopic Study on Fluorescence Enhancement by Plasmon Coupled Gold Nanorod Dimers Assembled on DNA Origami. *J. Phys. Chem. Lett.* **2015**, *6*, 2043−2049.

(31) Acuna, G. P.; Moller, F. M.; Holzmeister, P.; Beater, S.; Lalkens, B.; Tinnefeld, P. Fluorescence Enhancement at Docking Sites of DNA-Directed Self-Assembled Nanoantennas. *Science* **2012**, *338*, 506−10.

(32) Yuan, H.; Khatua, S.; Zijlstra, P.; Yorulmaz, M.; Orrit, M. Thousand-Fold Enhancement of Single-Molecule Fluorescence Near a Single Gold Nanorod. *Angew. Chem., Int. Ed.* **2013**, *52*, 1217−1221.

(33) Huang, B.; Bates, M.; Zhuang, X. W. Super-Resolution Fluorescence Microscopy. *Annu. Rev. Biochem.* **2009**, *78*, 993−1016.

(34) Huang, B.; Wang, W. Q.; Bates, M.; Zhuang, X. W. Three-Dimensional Super-Resolution Imaging by Stochastic Optical Reconstruction Microscopy. *Science* **2008**, *319*, 810−813.

(35) Whelan, D. R.; Bell, T. D. M. Super-Resolution Single-Molecule Localization Microscopy: Tricks of the Trade. *J. Phys. Chem. Lett.* **2015**, *6*, 374−382.

(36) Roeffaers, M. B. J.; De Cremer, G.; Libeert, J.; Ameloot, R.; Dedecker, P.; Bons, A. J.; Buckins, M.; Martens, J. A.; Sels, B. F.; De Vos, D. E.; Hofkens, J. Super-Resolution Reactivity Mapping of Nanostructured Catalyst Particles. *Angew. Chem., Int. Ed.* **2009**, *48*, 9285−9289.

(37) Zhou, X. C.; Andoy, N. M.; Liu, G. K.; Choudhary, E.; Han, K. S.; Shen, H.; Chen, P. Quantitative Super-Resolution Imaging Uncovers Reactivity Patterns on Single Nanocatalysts. *Nat. Nanotechnol.* **2012**, *7*, 237−241.

(38) Cang, H.; Labno, A.; Lu, C. G.; Yin, X. B.; Liu, M.; Gladden, C.; Liu, Y. M.; Zhang, X. Probing the Electromagnetic Field of a 15-Nanometre Hotspot by Single Molecule Imaging. *Nature* **2011**, *469*, 385−388.

(39) Blythe, K. L.; Titus, E. J.; Willets, K. A. Triplet-State-Mediated Super-Resolution Imaging of Fluorophore-Labeled Gold Nanorods. *ChemPhysChem* **2014**, *15*, 784−793.

(40) Weber, M. L.; Litz, J. P.; Masiello, D. J.; Willets, K. A. Super-Resolution Imaging Reveals a Difference between SERS and Luminescence Centroids. *ACS Nano* **2012**, *6*, 1839−1848.

(41) Stranahan, S. M.; Willets, K. A. Super-resolution Optical Imaging of Single-Molecule SERS Hot Spots. *Nano Lett.* **2010**, *10*, 3777−3784.

(42) Donehue, J. E.; Wertz, E.; Talicska, C. N.; Biteen, J. S. Plasmon-Enhanced Brightness and Photostability from Single Fluorescent Proteins Coupled to Gold Nanorods. *J. Phys. Chem. C* **2014**, *118*, 15027−15035.

(43) Lin, H. Z.; Centeno, S. P.; Su, L.; Kenens, B.; Rocha, S.; Sliwa, M.; Hofkens, J.; Uji-i, H. Mapping of Surface-Enhanced Fluorescence on Metal Nanoparticles using Super-Resolution Photoactivation Localization Microscopy. *ChemPhysChem* **2012**, *13*, 973−981.

(44) Su, L.; Lu, G.; Kenens, B.; Rocha, S.; Fron, E.; Yuan, H.; Chen, C.; Van Dorpe, P.; Roeffaers, M. B. J.; Mizuno, H.; Hofkens, J.; Hutchison, J. A.; Uji-i, H. Visualization of Molecular Fluorescence Point Spread Functions via Remote Excitation Switching Fluorescence Microscopy. *Nat. Commun.* **2015**, *6*, 6287.

(45) Blythe, K. L.; Titus, E. J.; Willets, K. A. Comparing the Accuracy of Reconstructed Image Size in Super-Resolution Imaging of Fluorophore-Labeled Gold Nanorods Using Different Fit Models. *J. Phys. Chem. C* **2015**, *119*, 19333−19343.

(46) Wertz, E.; Isaacoff, B. P.; Flynn, J. D.; Biteen, J. S. Single-Molecule Super-Resolution Microscopy Reveals How Light Couples

to a Plasmonic Nanoantenna on the Nanometer Scale. *Nano Lett.* **2015**, *15*, 2662−2670.

(47) Dedecker, P.; Muls, B.; Deres, A.; Uji-i, H.; Hotta, J.; Sliwa, M.; Soumillion, J. P.; Mullen, K.; Enderlein, J.; Hofkens, J. Defocused Wide-field Imaging Unravels Structural and Temporal Heterogeneity in Complex Systems. *Adv. Mater.* **2009**, *21*, 1079−1090.

(48) Li, T.; Li, Q.; Xu, Y.; Chen, X. J.; Dai, Q. F.; Liu, H. Y.; Lan, S.; Tie, S. L.; Wu, L. J. Three-Dimensional Orientation Sensors by Defocused Imaging of Gold Nanorods through an Ordinary Wide-Field Microscope. *ACS Nano* **2012**, *6*, 1268−1277.

(49) Patra, D.; Gregor, I.; Enderlein, J.; Sauer, M. Defocused imaging of quantum-dot angular distribution of radiation. *Appl. Phys. Lett.* **2005**, *87*, 101103.

(50) Habuchi, S.; Oba, T.; Vacha, M. Multi-Beam Single-Molecule Defocused Fluorescence Imaging Reveals Local Anisotropic Nature of Polymer Thin Films. *Phys. Chem. Chem. Phys.* **2011**, *13*, 7001−7007.

(51) Uji-i, H.; Melnikov, S. M.; Deres, A.; Bergamini, G.; De Schryver, F.; Herrmann, A.; Mullen, K.; Enderlein, J.; Hofkens, J. Visualizing Spatial and Temporal Heterogeneity of Single Molecule Rotational Diffusion in a Glassy Polymer by Defocused Wide-Field Imaging. *Polymer* **2006**, *47*, 2511−2518.

(52) Yorulmaz, M.; Khatua, S.; Zijlstra, P.; Gaiduk, A.; Orrit, M. Luminescence Quantum Yield of Single Gold Nanorods. *Nano Lett.* **2012**, *12*, 4385−4391.

(53) Schubert, O.; Becker, J.; Carbone, L.; Khalavka, Y.; Provalska, T.; Zins, I.; Sonnichsen, C. Mapping the Polarization Pattern of Plasmon Modes Reveals Nanoparticle Symmetry. *Nano Lett.* **2008**, *8*, 2345−2350.

(54) Motegi, T.; Nabika, H.; Niidome, Y.; Murakoshi, K. Observation of Defocus Images of a Single Metal Nanorod. *J. Phys. Chem. C* **2013**, *117*, 2535−2540.

(55) Mohammadi, A.; Sandoghdar, V.; Agio, M. Gold nanorods and nanospheroids for enhancing spontaneous emission. *New J. Phys.* **2008**, *10*, 105015.

(56) Perez-Juste, J.; Pastoriza-Santos, I.; Liz-Marzan, L. M.; Mulvaney, P. Gold Nanorods: Synthesis, Characterization and Applications. *Coord. Chem. Rev.* **2005**, *249*, 1870−1901.

(57) Yuan, H.; Janssen, K. P. F.; Franklin, T.; Lu, G.; Su, L.; Gu, X.; Uji-i, H.; Roeffaers, M. B. J.; Hofkens, J. Reshaping Anisotropic Gold Nanoparticles through Oxidative Etching: the Role of the Surfactant and Nanoparticle Surface Curvature. *RSC Adv.* **2015**, *5*, 6829−6833.

(58) Sohn, K.; Kim, F.; Pradel, K. C.; Wu, J. S.; Peng, Y.; Zhou, F. M.; Huang, J. X. Construction of Evolutionary Tree for Morphological Engineering of Nanoparticles. *ACS Nano* **2009**, *3*, 2191−2198.

(59) Enderlein, J.; Toprak, E.; Selvin, P. R. Polarization Effect on Position Accuracy of Fluorophore Localization. *Opt. Express* **2006**, *14*, 8111−8120.

(60) Dempsey, G. T.; Vaughan, J. C.; Chen, K. H.; Bates, M.; Zhuang, X. Evaluation of Fluorophores for Optimal Performance in Localization-Based Super-Resolution Imaging. *Nat. Methods* **2011**, *8*, 1027−1036.

(61) Zijlstra, P.; Paulo, P. M. R.; Orrit, M. Optical Detection of Single Non-absorbing Molecules Using the Surface Plasmon Resonance of a Gold Nanorod. *Nat. Nanotechnol.* **2012**, *7*, 379−382.

(62) Johnson, P. B.; Christy, R. W. Optical Constants of the Noble Metals. *Phys. Rev. B* **1972**, *6*, 4370−4379.